

Atomistic simulations of Mg vacancy segregation to dislocation cores in forsterite

1 Richard Skelton ^{a,*} and Andrew M. Walker^b

2 ^a Research School of Earth Sciences, Australian National University, Canberra, ACT, 0200, Australia

3 (ORCID: 0000-0003-1583-2312)

4 ^b School of Earth and Environment, University of Leeds, Leeds, LS2 9JT, UK

5 (ORCID: 0000-0003-3121-3255)

6 * Corresponding author: richard.skelton@anu.edu.au

7 **Abstract** This manuscript is a non-peer reviewed preprint submitted to EarthArXiv. It has been submitted to "Contributions to Mineralogy and Petrology" for consideration for publication.

8 Interactions between dislocations in olivine and extrinsic cation vacancies created under hydrous or
9 oxidizing conditions may influence the rheology of the Earth's upper mantle. In this study, we use
10 atomic-scale simulations to calculate segregation energies for bare and protonated Mg vacancies to M1
11 and M2 sites in the core regions of [100](010) and [001](010) edge dislocations, and [100] and [001]
12 screw dislocations. Calculated segregation energies are different for the two symmetry distinct M sites.
13 The segregation energies calculated for the tightest binding M1 sites around [100] screw and [100]
14 (010) edge dislocations are comparable to those calculated for the tightest binding M2 sites.
15 Concentrations of M2 vacancy-related defects will thus be low in the core regions of these dislocations,
16 given the comparatively high energy of these defects in the bulk lattice. In contrast, segregation
17 energies for M2 defects to [001](010) edge dislocation cores are considerably lower than for equivalent
18 M1 defects, and M2 vacancy concentrations around these dislocations will be similar to M1 vacancy
19 concentrations. This means that the effect of magnesium vacancies on the mobility of the [001](010)

20 edge dislocation may be significantly different to the effect on the mobility of the other dislocations
21 considered.

22 **Keywords:** Forsterite; dislocation; point-defect segregation; atomistic simulation; cation vacancies

23 **1. Introduction**

24 Although nominally anhydrous, under the pressure and temperature conditions of the Earth's mantle,
25 olivine can incorporate modest quantities of water into its crystal structure, primarily as protonated
26 cation vacancies (e.g. Martin and Donnay, 1972; Bai and Kohlstedt, 1993; Kohlstedt et al., 1996). The
27 water solubility limit in olivine is sensitive to the water and oxygen fugacities, and also increases with
28 silica activity, consistent with incorporation via protonation of M site vacancies (Gaetani et al., 2014).
29 Protonated vacancies interact with dislocations in the olivine crystal lattice, and may preferentially
30 occupy atomic sites near such defects over sites in the bulk lattice, with the effect that vacancy-related
31 defect concentrations are potentially much greater in the core region of a dislocation than in the
32 unstrained bulk lattice. In extreme cases, impurity segregation can affect the bulk chemistry of
33 minerals, as for example in the formation of striped chemical zoning in olivine during low strain-rate
34 deformation, attributed to Fe^{2+} segregation to sub-grain boundaries formed by aligned arrays of edge
35 dislocations (Ando et al., 2001). High-resolution synchrotron images show that the concentration of
36 protonated defects in olivine is greatest around grain boundaries and cracks, demonstrating that these
37 defects in olivine will tend to segregate to locally strained regions of the crystal lattice (Sommer et al.,
38 2008), while hydrogen concentrations near [001] dislocations in water-saturated olivine can be
39 sufficiently great to induce climb dissociation of the dislocation core (Drury, 1991).

40 Interactions between point defects and dislocations can alter the mobility of the dislocation. Most
41 commonly, dislocations experience solute drag when immobile impurities segregate to dislocation

42 cores, pinning the dislocation in place and reducing strain rates accordingly (Cottrell and Bilby, 1949).
43 However, some defects can increase dislocation mobility in the glide creep regime by reducing the
44 Peierls barrier to glide, including vacancies in fcc Al (Lauzier et al., 1989; Lu and Kaxiras, 2002),
45 hydrogen in Fe (Taketomi et al., 2008), or interstitial O defects in UO_2 (Ashbee and Yust, 1982; Keller
46 et al., 1988). In olivine, interactions between water-related defects, occurring primarily as protonated
47 vacancies may facilitate deformation by increasing dislocation mobility in the dislocation climb-
48 controlled creep regime (e.g. Mackwell et al., 1985; Chen et al., 1998; Girard et al., 2013). Hydrous
49 defects are thought to reduce the Peierls stress, σ_p , required for dislocation glide, whose measured value
50 for hydrated olivine is $\sim 1.6\text{-}2.9$ GPa (Katayama and Karato, 2008), considerably lower than values
51 measured for dry olivine polycrystals, which range from at least 3.8 GPa (Idrissi et al., 2016) to as
52 much as ~ 15 GPa (Demouchy et al., 2013). Recent forced-oscillation measurements have suggested
53 that Mg vacancies, produced to charge balance the oxidation of Fe^{2+} to Fe^{3+} (Stocker and Smyth, 1978;
54 Nakamura and Schmalzried, 1983) may enhance attenuation in Fo_{90} olivine (Cline et al., 2018)..
55 Natural dunites deforming in the dislocation creep regime also show a moderate sensitivity to the
56 oxygen fugacity (Keefner et al., 2011). This suggests that bare cation vacancies may have a similar
57 influence on the mechanical properties of olivine as protonated cation vacancies.

58 The short length scales characteristic of impurity segregation to dislocation cores mean that it can be
59 difficult to study experimentally, although developments in the field of atom probe tomography mean
60 that it is now possible to visualize impurity clouds around dislocation lines (Miller et al., 2006;
61 Peterman et al., 2016). Theoretical modeling offers an alternative approach, allowing direct access to
62 the atomic scale and control over system chemistry. While interactions between dislocations and point
63 defects far from the dislocation line can be adequately modeled using linear elasticity theory, is the
64 dislocation core non-elastic, atomic-scale relaxation can be substantial. One way to model a dislocation

65 is to insert two or more dislocations into a 3D-periodic simulation cell, with their Burgers vectors \mathbf{b}
66 summing to zero to ensure continuity at the boundaries. Although this cell can be sufficiently small as
67 to make the use of *ab initio* methods practical, care must be taken to minimize dislocation-dislocation
68 interactions. An alternative is to embed a single dislocation in an isolated cluster of atoms with periodic
69 boundary conditions along the dislocation line (Walker et al., 2005a). Both the cluster-based (Walker et
70 al., 2005b) and supercell (Mahendran et al., 2017) approaches have been used to simulate [100] and
71 [001] screw dislocations in forsterite, producing comparable dislocation core structures, although the
72 latter study did not report core energies for either dislocation.

73 While atomistic modeling is a powerful tool for studying dislocations and their interactions with point
74 defects, there are several limitations that restrict its range of applicability. Firstly, obtaining a converged
75 dislocation core structure and energy may require the use of very large simulation cell, containing
76 many hundreds or thousands of atoms, for which the computational cost of using quantum chemical
77 methods such as DFT can be prohibitive. Instead, as in this study, interatomic potentials are more
78 commonly used, which are parameterized by fitting to experimental data or *ab initio* calculations. The
79 second problem is that the dislocation itself breaks the translational symmetry of the crystal, meaning
80 that interactions between point defects cannot be parametrized using any of the techniques available for
81 solid solutions, such as cluster expansion (Sanchez et al., 1984) or Special Quasirandom Structures
82 (Zunger et al., 1990), and the dislocation energy must be obtained from fully atomistic calculations. In
83 practice, this limits calculations to the dilute limit.

84 In this study, we use the cluster-based approach to determine segregation energies for bare and
85 protonated cation vacancies to dislocation cores in the forsterite (Mg_2SiO_4) end-member of the olivine
86 solid solution. Since the silica activity in mantle peridotites is high, Mg vacancies are expected to be
87 more abundant than Si vacancies. Consequently, we consider only Mg vacancies on the two symmetry

88 distinct M sites, labeled M1 and M2. At low pressure, the easiest slip system in olivine is [100](010),
89 but the [001](010) slip system becomes more active at high pressure (Couvy et al., 2004; Hilairet et al.,
90 2012). Here, we use popular and well-tested empirical interatomic potential to calculate low energy
91 core structures for the [100](010) and [001](010) edge and [100] and [001] screw dislocation.
92 Segregation energies are calculated for bare and protonated M1 and M2 vacancies, written $\{V_{M1}\}^{\prime\prime}$,
93 $\{2H_{M1}\}^X$, $\{V_{M2}\}^X$ and $\{2H_{M2}\}^X$ in the Kröger-Vink notation (Kröger and Vink, 1956), to sites within the
94 core regions of these dislocations. Energies for the different defects are compared to elucidate the effect
95 of site occupation and hydrogen fugacity on the interaction between Mg vacancies to dislocations. In
96 the bulk, M1 vacancies are energetically more favorable than M2 vacancies in the bulk lattice
97 (Brodholt, 1997), but this may be different near dislocation cores, which may have implications for
98 olivine rheology in dislocation-controlled creep regimes, as well as for Mg diffusion in crystals with
99 high dislocation density.

100 2. Computational methods

101 Dislocation core structures and segregation energies were calculated using the cluster-based approach,
102 in which an isolated dislocation is inserted at the axis of a 1D-periodic cylinder of atoms (Sinclair,
103 1971; Walker et al., 2005ab). The starting coordinates for the atoms are determined from the elastic
104 displacement field $\mathbf{u}(\mathbf{r})$ calculated using the sextic formulation for a dislocation in an anisotropic
105 medium (Stroh, 1958). For edge dislocations, this is a non-conservative algorithm and atoms must be
106 removed from the simulation cell to obtain a physically reasonable initial dislocation structure. To do
107 this, a branch cut is created that is normal to both the Burgers and dislocation line vectors. Any atoms
108 that are displaced across this branch cut by the displacement field $\mathbf{u}(\mathbf{r})$ are deleted. Atoms in close
109 proximity to the branch cut are merged with any nearby atoms, if the distance between them falls below
110 a specified threshold d_{\min} . The cluster of atoms is subsequently divided into two concentric regions,

111 with radii R_I and R_{II} . During the geometry optimization step, atoms in the inner region (region I) are
 112 permitted to relax freely, while those in the outer region (region II) are held fixed at the coordinates
 113 predicted using the elastic displacement field.

114 The total excess energy per unit length, E_{dis} , contained within radius r of an isolated dislocation is

$$115 \quad E_{dis}(r) = E_{core} + \frac{Kb^2}{4\pi} \log(r/r_c) \quad , \quad (1)$$

116 where K is the elastic energy coefficient and depends on the dislocation geometry and elastic constants
 117 C_{ij} , E_{core} is the energy contained within the core region (termed the core energy), and r_c is the radius of
 118 the dislocation core, within which the displacement field diverges from the predictions of linear
 119 elasticity. The core radius r_c is an undetermined parameter, whose value cannot be determined from the
 120 radial excess energy of the dislocation. Its value must be chosen in order to set a gauge for the core
 121 energy. In this study, we use a core radius of $2b$, where b is the absolute magnitude of the Burgers
 122 vector.

123 The core energy is determined from atomistic cluster-based simulations by fitting equation (1) to the
 124 calculated radial dependence of the excess energy, which is the difference between the energy of a
 125 cluster containing the dislocation and a reference system containing an identical number of atoms. E_{core}
 126 is also the excess energy of the dislocation at $r = r_c$. The excess energy is calculated from the energies
 127 of the individual atoms as

$$128 \quad E_{excess}(r) = E_{dis}(r) - \sum_{species} n_{species}(r) E_{species} \quad , \quad (2)$$

129 where $E_{dis}(r)$ is the total energy of the atoms within r of the dislocation line, the sum runs over the
130 different atomic species present, $n_{species}(r)$ gives the number of atoms of each species within r , and $E_{species}$
131 is the energy of the species in the bulk lattice. This is equal to

$$132 \quad E_{species} = 1/2(E_{supercell} + E_{isolated} - E_{vac}) \quad , \quad (3)$$

133 where E_{vac} is the energy of a supercell from which one atom of the specified type has been removed,
134 without relaxing the coordinates of the remaining atoms, $E_{supercell}$ is the energy of the supercell without a
135 vacancy, and $E_{isolated}$ is the energy of an isolated atom of the specified type. In single-component
136 crystals, this is identical to the energy of the unit cell divided by the number of atoms it contains.

137 The core energy and core displacement field of a dislocation in a two-region cluster depends on the
138 radius of the relaxed region. A region I radius $R_I = 25 \text{ \AA}$ was sufficient to guarantee convergence of the
139 calculated core energies of the [100](010) edge and [100] and [001] screw dislocations to $<10 \text{ meV/\AA}$,
140 while a larger region I with radius $R_I = 35 \text{ \AA}$ was needed to achieve similar precision for the [001](010)
141 edge dislocation. The coulomb energy was calculated using the Wolf summation (Wolf et al., 1999),
142 which uses a charge neutralizing term to guarantee convergence of the energy at a finite distance. A
143 cutoff range of $r_{cut} = 15 \text{ \AA}$ and damping parameter $\xi = 0.2 \text{ \AA}^{-1}$ were used, giving lattice parameters and
144 elastic constants that differ from the values calculated using the Ewald method by $<1\%$. As electrostatic
145 interaction between ions is truncated at r_{cut} , the region II radius R_{II} of $R_I + r_{cut}$ is used for all cluster
146 calculations.

147 Due to the large size of the simulation cell, all calculations are performed using empirical interatomic
148 potentials in the program GULP (Gale, 1997; Gale and Rohl, 2003). The interatomic potentials used are
149 from the THB1 model, which was parameterized by fitting to experimental data (Sanders et al., 1984;

150 Lewis and Catlow, 1985), and reproduces the physical properties of forsterite with reasonable accuracy
 151 (Price et al., 1987). Following Wright and Catlow (1994), we model protonated vacancies using the
 152 parameters developed by Schröder et al. (1992) to treat (OH)⁻ groups in zeolite, incorporating the
 153 subsequent modifications made to the Morse potential by Gatzemeier and Wright (2006). This
 154 potential, labeled THB1, has been widely used to model point and extended defects in forsterite,
 155 including Mg point defects (Walker et al., 2009), surface structures and energetics (de Leeuw et al.,
 156 2000), and screw dislocation core structures and energies (Walker et al., 2005b).

157 In cluster calculations, the segregation energy E_{seg} of a single point defect at an atomic site in a
 158 dislocation core is determined by calculating the excess energy ΔE_{dis} of a point defect of the specified
 159 type embedded it in a simulation cell whose length is a multiple of the unit cell edge parallel to the
 160 dislocation line vector, ξ , and comparing it with the excess energy ΔE_{perf} of an isolated defect in the
 161 bulk lattice, taken here to be the excess energy ΔE_{perf} of a point defect embedded in a 3D-periodic
 162 supercell of the material. This is equivalent to

$$163 \quad E_{seg} = \left(E_{dfct+dis} - E_{dis} \right) - \left(E_{dfct+supercell} - E_{supercell} \right) , \quad (4)$$

164 where E_{dis} is the energy of a cluster containing a dislocation, $E_{dfct+dis}$ is the energy of that same cluster
 165 with a single point defect inserted, $E_{supercell}$ is the energy of a defect-free 3D-periodic supercell, and
 166 $E_{dfct+supercell}$ is the energy of a supercell containing a point defect. Negative segregation energies indicates
 167 that the point defect will tend to bind to this site to lower the total energy of the system, while positive
 168 segregation energies indicate the reverse.

169 $\{V_{M1}\}''$ and $\{V_{M2}\}''$ defects are inserted into a simulation by removing atoms of the specified type. As
 170 these defects are charged, a charge-neutralizing background was applied to the simulation cell, to

171 maintain over charge neutrality. In addition to calculating segregation energies for bare Mg vacancies,
172 segregation energies were also calculated for protonated Mg site vacancies. Constructing a $\{2H_{Mg}\}^x$
173 defect involves not only deletion of the Mg ion occupying the specified M site, and its replacement
174 with two H ions, but also the replacement of two of the O ions around the site with oxygen ions using
175 the hydroxyl potential. There are three symmetrically distinct O sites in olivine labeled O1, O2, and
176 O3, leading a large number of possible configurations of the $\{2H_{M1}\}^x$ and $\{2H_{M2}\}^x$ defects. For both
177 protonated defects, we use the configuration predicted by Walker et al. (2006) to have the lowest
178 energy. In a protonated M1 vacancy, the hydrogen atoms are bonded to oxygen in the O2 site, while the
179 hydrogen atoms in a protonated M2 vacancy are bonded to oxygen atoms on the O2 and O3 sites.

180 The segregation energies for the tightest binding site of the $\{V_{M1}\}''$, $\{V_{M2}\}''$, $\{2H_{M1}\}^x$, and $\{2H_{M2}\}^x$
181 defects for all four dislocations were converged to <0.05 eV by using supercells with length $n = 3$. The
182 distance between a point defect and its closest periodic image is thus 17.960 Å for dislocations with
183 line vector [001] and 14.346 Å for those with line vector [100]. Excess energies of isolated empty and
184 protonated M-site vacancies were calculated using a simulation cell with dimensions $4ax2bx4c$, where
185 a , b , and c are the forsterite cell parameters, sufficiently large to guarantee convergence to within the
186 tolerance specified for point defects in 1D-periodic clusters.

187 **3. Dislocation core properties**

188 The energy of a given dislocation depends on its coordinates within the crystallographic plane normal
189 to ξ . For each of the dislocations considered in this study, there are several possible symmetrically
190 distinct origins (labeled in Fig. 1). In the case of edge dislocations, which also break any rotational
191 symmetry of the crystal about the line vector ξ , the number of symmetrically distinct origins for a
192 dislocation can be even higher. Core energies for the most stable configuration found for each

193 dislocation obtained by fitting the computed radial variation of the excess energy (Fig. 3) to equation
194 (1) are reported in Table 1. Also shown are their associated elastic energy coefficients K , which are
195 determined from the elastic constant C_{ij} using the Stroh sextic theory (Stroh, 1958). The lowest energy
196 core structures found are displayed in Fig. 2.

197 [100] screw dislocations have higher core energies, E_{core} , than [001] screw dislocations. The calculated
198 core energies for the [100](010) and [001](010) edge dislocation slip systems are comparable.
199 However, the core radius r_c depends on the length of the Burgers vector, which is shorter for the [100]
200 (010) edge dislocation, and E_{core} therefore corresponds to the energy of a smaller region. As can be seen
201 in Table 1, the [001] screw dislocation has the lowest core energy (1.50 eV/Å) and elastic energy
202 coefficient (57.4 GPa) among the dislocations considered in this study. Consistent with these results,
203 atomistic calculations of generalized stacking fault energies have shown that both the relative volume
204 change of SiO₄ tetrahedra and the displacement of atoms away from the fault surface, which serve as
205 measures of nonelastic strain, are greater for [100](010) slip than [001](010) slip (Durinck et al., 2005).
206 It follows that [100](010) dislocations should be expected to have higher core energies than [001](010)
207 dislocations.

208 Equilibrium core structures for the [100](010) and [001](010) edge dislocations are shown in Fig. 2ab.
209 As can be seen in Fig. 2a, the [100](010) edge dislocation has an asymmetric core structure, a
210 consequence of the absence of mirror planes parallel to [100]. The algorithm for creating an edge
211 dislocation creates something similar to a vacant M2 site near the [100](010) dislocation line. Inserting
212 an Mg atom at this site increases the core energy by 0.2 eV/Å. As a consequence, the [100](010) edge
213 dislocation has an empty channel parallel to ξ , causing the oxygen ions closest to the dislocation line to
214 be under-coordinated. In contrast to the [100](010) edge dislocation, the stable core structure of the

215 [001](010) edge dislocation is symmetric, due to the existence of mirror planes parallel to (001) located
216 at $z = 0.25$ and $z = 0.75$, passing through the row of Si atoms parallel to [010]. Both edge dislocations
217 lie on the median planes of the M_2O_6 polyhedra ($y = 0.25/0.75$). This is consistent with quantum
218 mechanical calculations of generalized stacking fault energies, which find that ideal shear stresses for
219 [100](010) and [001](010) slip are lowest when slip is localized at $y = 0.25$ (Durinck et al., 2005). The
220 Peierls stresses for dislocations gliding on (010) are similarly lowest when glide is on the plane at $y =$
221 0.25 (Durinck et al., 2007).

222 For the [100] screw dislocation, we find that the origin of the most stable core structure is (0.5, 0.25),
223 halfway between adjacent M2 sites (labeled site C in Fig. 1a), which has a calculated core energy of
224 $E_{\text{core}} = 1.78 \text{ eV/\AA}$. This core structure was also reported by Mahendran et al. (2017), who used the
225 alternative supercell approach. Earlier work using the cluster-based approach, by contrast, found that
226 the dislocation centered on the M1 site has a lower energy (Walker et al., 2005b), for which we
227 compute a relatively high core energy of 1.97 eV/\AA . The discrepancy is likely due to the fact that
228 Walker et al. (2005b) searched for the minimum energy core structure using single point energy
229 calculations at each possible core position, whereas the core structures were relaxed in this study. Local
230 atomic-scale structure thus has a determining effect on the relative stability of the different core
231 configurations for the [100] screw dislocation in forsterite.

232 Whereas other dislocations gliding on (010) are located on the median plane of the sheet of M_2O_6
233 octahedra, the most stable core structure of the [001] screw dislocation is centered on the column of
234 M_1O_6 polyhedra running parallel to [001] (labeled site D in Fig. 1b), consistent with previous
235 theoretical calculations (Walker et al., 2005b; Mahendran et al., 2017). As found in previous studies
236 (Carrez et al., 2008), the [001] screw dislocation has a non-planar core. This is can be seen clearly in
237 the sub-periodic modulation of the displacement \mathbf{u} of M1 sites located in the lattice plane a distance

238 $1/2b$ above and below the glide plane. These atoms are displaced normal to the (010) glide plane, with
239 the sense of this displacement alternating along [001] (see Fig. 2d). The SiO_4 tetrahedra in this plane
240 undergo significant rotation, with the sign of this rotation alternating in the fashion as the sign of the
241 displacement of neighboring M1 sites. This modulation causes the two-fold rotation center at $z = 0.5$,
242 where z is the coordinate along the dislocation line, to disappear. In what follows, the region in which
243 $0.0 \leq z < 0.5$ is referred to as the "lower" region, and the region with z satisfying $0.5 \leq z < 1.0$ as the
244 "upper" region. In this labeling scheme, the lower region corresponds to those M1 sites that relax away
245 from the (010) glide plane, and the upper region to the sites that relax toward it.

246 **4. Segregation of Mg vacancies to dislocations**

247 *4.1 Excess energies of defects in the bulk lattice*

248 Segregation energies are calculated from equation (4), which requires the excess energy of a point
249 defect in the bulk lattice. This excess energy is defined as the difference between the energies of
250 forsterite supercells of the same size, with and without a point defect. The excess energy of an $\{\text{V}_{\text{M1}}\}$
251 defect, corrected for the interactions between charged defects, is 24.0 eV, while a $\{\text{V}_{\text{M2}}\}$ defect has a
252 modestly higher excess energy of 25.9 eV, reflecting the lower energy of a magnesium ion in M2 site.
253 Similarly, the excess energy of a $\{2\text{H}_{\text{M2}}\}^{\text{X}}$ defect in the bulk lattice is 41.8 eV, significantly greater than
254 the 39.4 eV excess energy calculated for the $\{2\text{H}_{\text{M1}}\}^{\text{X}}$ defect.

255 Creating an M1 vacancy, whether protonated or bare, is thus more energetically favorable than creating
256 an M2 vacancy. $\Delta H_{\text{M1} \rightarrow \text{M2}}$, the enthalpy required to exchange an Mg vacancy between the M1 and M2
257 sub-lattices is 1.9 eV, identical to previous values of $\Delta H_{\text{M1} \rightarrow \text{M2}}$ calculated using empirical potentials
258 (Jaoul et al., 1995; Walker et al., 2009), but higher than the 0.81 eV energy difference predicted by DFT

259 calculations (Brodholt, 1997). The energy difference $\Delta H_{M1 \rightarrow M2}$ between the $\{2H_{M1}\}^X$ and $\{2H_{M2}\}^X$
260 defects, at 2.4 eV, is even greater than that for bare vacancies. As the relative concentrations of
261 vacancies on the two sites depends exponentially on $\Delta H_{M1 \rightarrow M2}$, M1 vacancies, whether bare or
262 protonated, will be considerably more abundant than similar M2 vacancy-related defects in the bulk
263 lattice.

264 4.2 Segregation of M1 vacancies

265 The segregation energy for the $\{V_{M1}\}''$ defect around a [100](010) edge dislocation is lowest for the
266 three sites located directly below the dislocation line (Fig. 4a). The $\{V_{M1}\}''$ defect binds particularly
267 tightly to the site directly below the glide plane, which has a segregation energy of -3.00 eV.
268 Segregation energies for the $\{2H_{M1}\}^X$ defect are similarly lowest for the three sites immediately below
269 the glide plane, although their segregation energies are more similar in value. $E_{seg} = -2.30$ eV for the
270 site directly below the glide plane. For both defects, segregation energies decrease rapidly with distance
271 from the dislocation line.

272 Segregation energies for M1 defects around [001](010) edge dislocations are shown in Fig. 5. $\{V_{M1}\}''$
273 defects bind to the sites immediately above the glide plane of [001](010) edge dislocations, with
274 segregation energy -1.74 eV. As was found for $\{V_{M1}\}''$ around the [100](010) edge dislocation,
275 segregation energies increase markedly away from the most stable binding site; the next lowest energy
276 is -1.05 eV, corresponding to the M1 sites on either side of the tightest binding sites. As was found for
277 [100](010) dislocations, $\{2H_{M1}\}^X$ defects segregating to [001](010) edge dislocations preferentially
278 bind to sites directly below the glide plane and close to the dislocation line, albeit with considerably
279 higher segregation energies than found for [100](010) edge dislocations. For the tightest binding site,

280 which is located directly below the glide plane and on either side of the dislocation line, $E_{seg} = -1.08$ eV,
281 and segregation energies are only marginally higher for M1 sites above the glide plane.

282 The calculated minimum segregation energies for M1 vacancies binding to screw dislocation cores are
283 higher than those for the edge dislocations, consistent with the lower stresses induced by a screw
284 dislocation. For the [100] screw dislocation, the low energy sites are distributed radially around the
285 dislocation core (Fig. 6), with the tightest binding sites being those closest to the (010) glide plane. The
286 tightest binding sites for the $\{V_{M1}\}''$ defect, at $\mathbf{r} \approx \pm[(1/2)\mathbf{c}+(1/4)\mathbf{b}]$ (\mathbf{b} in this context referring to the
287 unit cell length rather than the Burgers vector), have $E_{seg} = -0.87$ eV, while $E_{seg} = -0.81$ eV for the next
288 most tightly bound sites, which are located at $\mathbf{r} \approx \pm[(1/2)\mathbf{c}-(1/4)\mathbf{b}]$. However, the sites closest to the
289 dislocation line have comparatively high segregation energies (-0.20 eV). Comparing Fig. 6a and Fig.
290 6b, it can be readily seen that $\{2H_{M1}\}^X$ defects show greater site selectivity than $\{V_{M1}\}''$ defects, as the
291 segregation energies for the sites at $\mathbf{r} \approx \pm[(1/2)\mathbf{c}-(1/4)\mathbf{b}]$, -0.99 eV, are considerably lower than those
292 computed for any other site, while those at $\mathbf{r} \approx \pm[(1/2)\mathbf{c}+(1/4)\mathbf{b}]$ have considerably higher energies (-
293 0.35 eV), comparable to the -0.40 eV of the M1 sites closest to the dislocation line. Segregation
294 energies for $\{2H_{M1}\}^X$ defects decrease more rapidly with distance from dislocation line than do
295 segregation energies calculated for bare M1 vacancies.

296 Segregation energies for defects around the [001] screw dislocation (Fig. 7) depend not only on their
297 location in the plane normal to the line vector ξ , but also on their position along the ξ , due to the
298 modulation of the crystal structure along the dislocation line. For the bare M1 vacancy the lowest
299 segregation energy site is -0.77 eV within the lower region, compared with -0.61 eV in the upper
300 region. Segregation energies for the $\{2H_{M1}\}^X$ defect are more sensitive to location along the dislocation
301 line. $E_{seg} = -0.89$ eV for the tightest binding site in the lower region, while the lowest segregation

302 energy found for any site in the upper region is only -0.62 eV. For both bare and protonated defects, is
303 generally lower for sites in the lower region, and E_{seg} can be positive for sites in the upper region,
304 particularly the site through which the dislocation line passes. Defect concentrations will be lower in
305 this region than in the bulk lattice. Segregation energies for M1 vacancy-related defects in the upper
306 and lower regions of the [001] screw dislocation are anti-correlated, which may inhibit pipe diffusion
307 along this dislocation as vacancy migration entails successive jumps between high and low segregation
308 energy sites.

309 4.3 Segregation of M2 vacancies

310 The lowest segregation energy site for $\{V_{M2}\}''$ around the [100](010) edge dislocation is not at the glide
311 plane, but at $x = 0$ on the first sheet of M_2O_6 octahedra below the dislocation (Fig. 4). The segregation
312 energy of the most stable binding site (-3.93 eV) is considerably lower than that calculated at any other
313 location in the dislocation core, matching the behavior found for $\{V_{M1}\}''$ defects segregating to this
314 dislocation. The energies of the next tightest binding sites, those immediately adjacent to the
315 dislocation on the glide plane, are considerably higher, with $E_{seg} = -1.4$ eV. As was found for the M1
316 defects segregating to this dislocation, the segregation energy surface of the $\{2H_{M2}\}^X$ defect is
317 profoundly different to that of the $\{V_{M2}\}''$ defect. Unlike $\{V_{M2}\}''$, $\{2H_{M2}\}^X$ binds to sites near the glide
318 plane, with the lowest energies found for the four sites closest to the dislocation line. The two sites
319 closest to the dislocation line, which are above the glide plane, have $E_{seg} = -1.53$ eV, while $E_{seg} = -1.82$
320 eV for the two sites below the glide plane. Above the glide plane, segregation energies rapidly decay to
321 zero.

322 The tightest binding sites for $\{V_{M2}\}''$ defects segregating to [001](010) edge dislocations are in the
323 sheet of M_2O_6 octahedra above the glide plane (Fig. 5). For these sites, the segregation energy is -3.64

324 eV. The M2 site closest to the dislocation line has the next lowest energy, with $E_{seg} = -3.40$ eV. The
325 segregation energy for $\{2H_{M2}\}^x$ defects is lowest for the site at $x = 0$ is the sheet of $M2O_6$ octahedra
326 below the glide plane, for which $E_{seg} = -3.07$ eV. Unlike $\{V_{M2}\}''$ defects, segregation of $\{2H_{M2}\}^x$
327 defects to the M2 site closest to the dislocation line is comparatively unfavorable, with $E_{seg} = -0.70$ eV
328 for this site.

329 The low energy sites for $\{V_{M2}\}''$ and $\{2H_{M2}\}^x$ defects around the [100] screw dislocation are distributed
330 radially around the dislocation line (Fig. 6). However, for both defects the tightest binding sites are
331 located near the (010) glide plane. The energy for segregation of $\{V_{M2}\}''$ defects to the sites closest to
332 the dislocation line is -1.74 eV. The lowest segregation energies correspond to the next closest sites to
333 the dislocation line, for which $E_{seg} = -1.91$ eV. For protonated M2 vacancies, the sites immediately
334 adjacent to the dislocation line have the lowest energy, with $E_{seg} = -2.46$ eV. Segregation energies for
335 protonated vacancies increase more markedly with distance from the dislocation line than for bare M2
336 vacancies, and E_{seg} is only -1.39 eV for the next tightest binding site.

337 As was found for defects on the M1 sub-lattice around [001] screw dislocations, M2 segregation
338 energies vary along the dislocation line (Fig. 7). The sites for which the segregation energy of $\{V_{M2}\}''$ is
339 a minimum are found in the lower region. For these sites, $E_{seg} = -1.89$ eV, whereas the lowest
340 segregation energy for any site in the upper region is -1.06 eV. At upper mantle temperatures, the
341 concentration of $\{V_{M2}\}''$ defects will therefore be orders magnitude greater in the lower region than the
342 upper region, due to the exponential variation of relative concentrations on ΔH . For $\{2H_{M2}\}^x$ defects,
343 the six sites closest to the dislocation line have nearly identical segregation energies
344 (approximately -1.73 eV). In contrast to $\{V_{M2}\}''$ defects, the minimum energies in each region are

345 comparable, and $\{2H_{M2}\}^x$ bind as strongly to sites in the upper region as they do to sites in the lower
346 region.

347 5. Discussion

348 5.1 Comparing segregation energies for M1 and M2 defects

349 For all dislocations considered in this study, $\{V_{M2}\}''$ defects bind more tightly to core sites than $\{V_{M1}\}''$
350 defects. The difference between the minimum segregation energies for the two defects around a [100]
351 (010) edge dislocation is 0.93 eV. Comparable values of 1.04 and 1.18 eV are found for the [100] and
352 [001] screw dislocations, respectively. Except in the case of [100](010) edge dislocations, for which the
353 minimum segregation energy for the $\{2H_{M2}\}^x$ defect is 0.48 eV higher than that for the $\{2H_{M1}\}^x$ defect,
354 $\{2H_{M2}\}^x$ defects bind more strongly to dislocation cores, relative to the equivalent defect in the
355 unstrained lattice, than $\{2H_{M1}\}^x$ defects. M2 vacancy-related defects will be more strongly
356 concentrated near dislocation cores, relative to the bulk, than M1 defects. However, the lower absolute
357 energies of M1 vacancies mean that these defects will remain more abundant near dislocation cores
358 than M2 vacancies. The ratio of defect concentrations on the two sites, $[\{V_{M1}\}'']/[\{V_{M2}\}'']$ will
359 nevertheless still be lower near a dislocation than in the bulk lattice, as will the ratio $[\{2H_{M1}\}^x]/$
360 $[\{2H_{M2}\}^x]$, except around [100](010) edge dislocations.

361 However, while this means that the concentration of M2 vacancies, relative to M1 vacancies, is greater
362 in the vicinity of a dislocation core than in the bulk, this does not necessarily imply that they are lower
363 energy. Indeed, only in the case of [001](010) edge dislocations are the differences between the lowest
364 segregation energies of the $\{V_{M1}\}''$ and $\{V_{M2}\}''$ defects comparable to $\Delta H_{M1 \rightarrow M2}$ for the bulk lattice. The
365 energy difference for protonated M1 and M2 vacancies is lower than the bulk $\Delta H_{M1 \rightarrow M2}$ for all four

366 dislocations, so that creation of a protonated M1 vacancy near the dislocation core is still more
367 favorable than creation of a protonated M2 vacancy. Assuming that vacancy-related defects can
368 lubricate glide of dislocations in olivine, it is probable that the effect will vary with the distance of the
369 vacant site from the glide plane. In forsterite, this implies that M2 vacancies will have a greater
370 lubrication effect for dislocations gliding on (010) than M1 vacancies, as glide occurs primarily on the
371 (010)-parallel sheet of M_2O_6 octahedra. However, as shown here, with the exception of the [001](010)
372 edge dislocation, M2 vacancies are much less abundant than M1 vacancies near dislocation cores,
373 which could limit the magnitude of the glide lubrication effect.

374 The [001](010) edge dislocation represents a partial exception, as $\{V_{M_2}\}''$ defects bind particularly
375 strongly to the core sites of this dislocations. The segregation energy (relative to an equivalent defect in
376 the bulk) of the tightest binding site for $\{V_{M_2}\}''$ defects in the core region of this dislocation is 1.9 eV
377 lower than that of the tightest binding M1 site, comparable to the value of $\Delta H_{M_1 \rightarrow M_2}$ in the bulk lattice
378 environment. This means that absolute energies for the $\{V_{M_1}\}''$ and $\{V_{M_2}\}''$ defects segregating to
379 tightest binding sites in [001](010) edge dislocation cores are identical, and their concentrations close
380 the dislocation line will be similar. The low energy of the tightest binding M2 vacancy for this defect is
381 readily explained by the fact that the dislocation runs through an M2 site, so that the region of highest
382 strain coincides with an M2 site. The difference between the minimum segregation energies for
383 $\{2H_{M_2}\}^X$ and $\{2H_{M_1}\}^X$ defects around a [001](010) edge dislocation core is 2.0 eV. This is 0.4 eV lower
384 than the energy difference between the two defects in the absence of strain field. Consequently,
385 although hydrated M1 vacancies will be more abundant than M2 vacancies in the dislocation core, the
386 relative abundance of the latter will be far greater near the core of [001](010) edge dislocations than in
387 the bulk lattice.

388 5.2 Segregation energies of bare versus protonated defects

389 Among dislocations in forsterite gliding on (010), segregation energies are lower for edge than screw
390 dislocations and, in general, lower for dislocations with Burgers vector $\mathbf{b} = [100]$ than those with $\mathbf{b} =$
391 $[001]$. Considering only the sites with the lowest segregation energies, bare and protonated M1 and M2
392 vacancies should be more abundant near $[100](010)$ than $[001](010)$ edge dislocations, and with
393 generally higher concentrations for $[100]$ screw dislocations than $[001]$ screw dislocations. The spatial
394 distribution of segregation energies for protonated and bare M site vacancies for a specific dislocation
395 are similar. However, as noted in the previous section, the fine details of the segregation energy
396 surfaces can vary considerably and non-trivially between $\{V_{M1}\}''$ and $\{2H_{M1}\}^X$, and $\{V_{M2}\}''$ and
397 $\{2H_{M2}\}^X$. In this section, we will attempt to quantify the degree to which protonation changes
398 segregation energies.

399 The degree to which the segregation energies for two defects around a particular dislocation are similar
400 to one another can be quantified by computing a similarity measure for the segregation energy surfaces
401 around the dislocation core. One such measure is the cosine similarity measure, which is computed for
402 two vectors \mathbf{x}_1 and \mathbf{x}_2 as

$$403 \quad s_{12}(\mathbf{x}_1, \mathbf{x}_2) = \frac{\mathbf{x}_1 \cdot \mathbf{x}_2}{(\|\mathbf{x}_1\| \|\mathbf{x}_2\|)} \quad , \quad (5)$$

404 The similarity $s_{12} = -1$ when the vectors are anti-correlated, while $s_{12} = 1$ for perfectly correlated
405 vectors. The cosine similarity measure is widely used in data mining to compare data sets, with
406 applications ranging from facial verification (e.g. Nguyen and Bai, 2010), to comparing linguistic data
407 sets (e.g. Liao and Xu, 2015), and automated text classification (e.g. Song et al., 2009). Here, we
408 represent a segregation energy surface for a single point defect around a dislocation as a vector of

409 length equal to the number of sites, whose entries correspond to the segregation energies of each site.
410 Thus bare and protonated vacancies around the same dislocation can be compared provided that
411 segregation energies have been computed for the same list of sites, as is the case in this study.
412 However, the similarity measure cannot be straightforwardly compared between slip systems, as the list
413 of sites will be different. Computed values of s_{12} for the M1 and M2 sites within 15 Å of the dislocation
414 line are given in Table 3.

415 The similarity s_{12} of the M2 sub-lattice is strictly positive for all dislocations, meaning that the
416 segregation energies of $\{V_{M2}\}''$ and $\{2H_{M2}\}^x$ defects to dislocations in forsterite are invariably
417 positively correlated. For all four dislocations considered in this study, the cosine similarity measure is
418 positive, indicating a broad correlation between segregation energies of bare and protonated vacancies
419 on the same sub-lattice. Bare and protonated Mg vacancies around [100](010) edge dislocations have
420 relatively similar energies for both sub-lattices and, and $s_{12}(M1)$ is only ~3% greater than the
421 corresponding value for the M2 sub-lattice. Around [001](010) edge dislocations, s_{12} differs
422 considerably for defects on the two sub-lattices around [001](010) edge dislocations, with
423 $s_{12}(M1)/s_{12}(M2) = 1.20$. In contrast, the similarity measures computed using the calculated segregation
424 energy surfaces for screw dislocations are considerably greater on the M2 sub-lattice, with
425 $s_{12}(M2)/s_{12}(M1) = 1.14$ for [100] screw dislocations and 1.19 for [001] screw dislocation.

426 The [001] screw dislocation has a modulated core structure, and defects on M1 sites that are adjacent
427 along [001] have different segregation energies, as can be seen in Fig. 7. Considering the segregation
428 energies for the M1 sites at $y = 0.0$ (Fig. 7ab) and $y = 0.5$ (Fig. 7cd) separately, we find similarities $s_{12} =$
429 0.889 and $s_{12} = 0.44$. Thus, although $\{V_{M1}\}''$ and $\{2H_{M1}\}^x$ segregation energies are more strongly
430 correlated for the M1 sites which displace away from the (010) glide plane, they are only weakly
431 correlated for the M1 sites that are displaced towards the glide plane. As can be seen in Fig. 7, the

432 pattern of segregation energies for the M2 vacancies similarly varies between the upper and lower
433 regions of the [001] screw dislocation. However, the similarity measure varies much less between the
434 two regions for M2 vacancies than M1 vacancies, with $s_{12} = 0.87$ for sites in the lower region, and $s_{12} =$
435 0.94 in the upper region.

436 *5.3 Defect segregation and olivine deformation*

437 Vacancy-lubrication of dislocation glide has been reported in a range of different materials. Generalized
438 stacking fault energy (GSFE) parametrized Peierls-Nabarro calculations have suggested that interstitial
439 H may facilitate dislocation glide in Al meta (Lu et al. 2001), while the presence of interstitial O in
440 hyper-stoichiometric UO_2 (i.e. UO_{2+x} , $x > 0$) is known to reduce the critical resolved shear stress (Keller
441 et al. 1988), an effect attributed to interactions between the interstitial impurities and the dislocation
442 core (Ashbee and Yust, 1982). One possible explanation is that interactions between the dislocation
443 core and an adsorbed vacancy defect reduce the Peierls stress, although the precise mechanism remains
444 unclear. Deformation experiments in the glide-controlled creep regime show that the critical resolved
445 shear stress decreases from 3.8-15.0 GPa in dry olivine (Idrissi et al., 2016; Demouchy et al., 2013) to
446 1.6-2.9 GPa for olivine under water-saturated conditions (Katayama and Karato, 2008). This CRSS
447 represents the stress required for deformation at 0 K, and is referred to by Katayama and Karato as the
448 Peierls stress, although it actually represents a weighted average of the Peierls stresses for several
449 active slip systems.

450 The solubility limit of vacancy-related defects in the olivine crystal lattice is relatively high, and can
451 reach nearly 0.9 % for protonated vacancies at 12 GPa pressure (Smyth et al., 2006). However, these
452 concentrations are probably not sufficiently great to create Peierls stress reductions of the magnitude
453 reported by Katayama and Karato (2008). However, the strongly negative segregation energies

454 calculated for both edge and screw dislocations mean that the concentration of vacancy-related defects
455 will be many times greater in the dislocation core than in the bulk crystal lattice. It follows that the
456 influence of vacancy-related defects on the deformation of olivine in dislocation-controlled creep
457 regimes can be significant, even at low bulk concentrations. Moreover, $\{V_{M2}\}''$ and $\{2H_{M2}\}^x$ defects
458 were found to have considerably lower segregation energies than equivalent defects on the M1 sub-
459 lattice, and the relative abundance of M2 defects will be much higher in dislocation cores than in the
460 bulk lattice. This is significant, as M2 vacancies are expected to have the greatest influence on the
461 Peierls stress for dislocations gliding on (010), as these dislocations glide on the median plane of the
462 sheet of M_2O_6 octahedra.

463 **6. Conclusions**

464 Vacancy related defects are important for understanding the material properties of olivine. The addition
465 of small quantities of water to Fo_{90} olivine deforming in the glide creep regime increases strain rates,
466 indicating a reduction of the Peierls stress. This has been plausibly attributed to lubrication of
467 dislocation glide by protonated cation vacancies interacting with the dislocation, a process similar to
468 the vacancy lubrication phenomenon invoked to explain flow stress variations for a range of materials.
469 Concentrations of protonated vacancies or similar vacancy-related defects present at the dislocation
470 core need to be high for the lubrication effect to be substantial. However, H concentration in mantle
471 olivine is typically low, with <1000 ppm H/Si, although water contents may reach higher values in the
472 deep upper mantle. Ferric iron, an important source of bare vacancies in silicate minerals, has a
473 similarly low abundance, except in the most oxidized regions of the mantle (Kelley and Cottrell, 2009).
474 Consequently, vacancy lubrication is possible only if vacancy related defects bind strongly to sites
475 around dislocation cores.

476 In this study, we have used cluster-based computational simulations to compute segregation energies
477 for both bare and protonated Mg vacancies around dislocations in forsterite. These segregation energies
478 can be < -1.0 eV, suggesting that vacancy-related defect concentrations near the dislocation core may
479 be orders of magnitude higher than in the bulk lattice, especially at low to moderate temperature. These
480 are precisely the temperature conditions at which dislocation glide is most important for the
481 deformation of olivine. However, not all vacancies are equal and, while the energy of an $\{V_{M2}\}''$ or
482 $\{2H_{M2}\}^x$ defect is considerably lower near an edge or screw dislocation line than an equivalent defect
483 in the bulk lattice, Mg vacancies still preferentially occupy M1 sites near dislocations, as they do in the
484 bulk lattice. Thus, even though concentrations of vacancy related defects at the dislocation core may be
485 high, they may occupy sites whose ability to directly influence dislocation glide is limited. The easy
486 glide plane for dislocations gliding on (010) is the median plane of the sheet of M_2O_6 octahedra, and
487 M2 vacancies located this glide plane may play a critical role in lubricating dislocation glide. Such
488 strategically located vacancies are expected to be most abundant around [001](010) edge dislocations,
489 and any increase in the glide mobility is likely to be most significant for the [001](010) slip system.

490 **Acknowledgements**

491 AMW is grateful for support from the UK Natural Environment Research Council (NE/K008803/1 and
492 NE/M000044/1). RS is supported by an Australian Government Research Training Program (RTP)
493 Scholarship. Calculations were performed on the Terrawulf cluster, a computational facility supported
494 through the AuScope initiative. AuScope Ltd is funded under the National Collaborative Research
495 Infrastructure Strategy (NCRIS), an Australian Commonwealth Government Programme. This work
496 used the ARCHER UK National Supercomputing Service (<http://www.archer.ac.uk>). Ian Jackson is
497 thanked for his helpful comments.

499 **References**

- 500 Ando J, Shibata Y, Okajima Y, et al (2001) Striped iron zoning of olivine induced by dislocation creep
501 in deformed peridotites. *Nature* 414:893–895. doi: [10.1038/414893a](https://doi.org/10.1038/414893a)
- 502 Ashbee KHG, Yust CS (1982) A mechanism for the ease of slip in UO_2+x . *Journal of Nuclear*
503 *Materials* 110:246–250. doi: [10.1016/0022-3115\(82\)90152-0](https://doi.org/10.1016/0022-3115(82)90152-0)
- 504 Bai Q, Kohlstedt DL (1993) Effects of chemical environment on the solubility and incorporation
505 mechanism for hydrogen in olivine. *Phys Chem Minerals* 19:460–471. doi: [10.1007/BF00203186](https://doi.org/10.1007/BF00203186)
- 506 Brodholt J (1997) Ab initio calculations on point defects in forsterite (Mg_2SiO_4) and implications for
507 diffusion and creep. *American Mineralogist* 82:1049–1053. doi: [10.2138/am-1997-11-1201](https://doi.org/10.2138/am-1997-11-1201)
- 508 Carrez P, Walker AM, Metsue A, Cordier P (2008) Evidence from numerical modelling for 3D
509 spreading of [001] screw dislocations in Mg_2SiO_4 forsterite. *Philosophical Magazine* 88:2477–2485.
510 doi: [10.1080/14786430802363804](https://doi.org/10.1080/14786430802363804)
- 511 Chen J, Inoue T, Weidner DJ, et al (1998) Strength and water weakening of mantle minerals, olivine,
512 wadsleyite and ringwoodite. *Geophys Res Lett* 25:575–578. doi: [10.1029/98GL00043](https://doi.org/10.1029/98GL00043)
- 513 Cline II CJ, Faul UH, David EC, et al (2018) Redox-influenced seismic properties of upper-mantle
514 olivine. *Nature* 555:355–358. doi: [10.1038/nature25764](https://doi.org/10.1038/nature25764)
- 515 Cottrell AH, Bilby BA (1949) Dislocation Theory of Yielding and Strain Ageing of Iron. *Proc Phys Soc*
516 *A* 62:49. doi: [10.1088/0370-1298/62/1/308](https://doi.org/10.1088/0370-1298/62/1/308)
- 517 Couvy H, Frost DJ, Heidelbach F, et al (2004) Shear deformation experiments of forsterite at 11 GPa -
518 1400°C in the multianvil apparatus. *European Journal of Mineralogy* 16:877–889. doi: [10.1127/0935-
519 1221/2004/0016-0877](https://doi.org/10.1127/0935-1221/2004/0016-0877)
- 520 Demouchy S, Tommasi A, Boffa Ballaran T, Cordier P (2013) Low strength of Earth's uppermost
521 mantle inferred from tri-axial deformation experiments on dry olivine crystals. *Physics of the Earth and*
522 *Planetary Interiors* 220:37–49. doi: [10.1016/j.pepi.2013.04.008](https://doi.org/10.1016/j.pepi.2013.04.008)
- 523 Drury MR (1991) Hydration-induced climb dissociation of dislocations in naturally deformed mantle
524 olivine. *Phys Chem Minerals* 18:106–116. doi: [10.1007/BF00216603](https://doi.org/10.1007/BF00216603)

525 Durinck J, Legris A, Cordier P (2005) Pressure sensitivity of olivine slip systems: first-principle
526 calculations of generalised stacking faults. *Phys Chem Minerals* 32:646–654. doi: [10.1007/s00269-005-](https://doi.org/10.1007/s00269-005-0041-2)
527 [0041-2](https://doi.org/10.1007/s00269-005-0041-2)

528 Durinck J, Carrez P, Cordier P (2007) Application of the Peierls-Nabarro model to dislocations in
529 forsterite. *European Journal of Mineralogy* 19:631–639. doi: [10.1127/0935-1221/2007/0019-1757](https://doi.org/10.1127/0935-1221/2007/0019-1757)

530 Gaetani GA, O’Leary JA, Koga KT, et al (2014) Hydration of mantle olivine under variable water and
531 oxygen fugacity conditions. *Contrib Mineral Petrol* 167:965. doi: [10.1007/s00410-014-0965-y](https://doi.org/10.1007/s00410-014-0965-y)

532 Gale JD (1997) GULP: A computer program for the symmetry-adapted simulation of solids. *J Chem*
533 *Soc, Faraday Trans* 93:629–637. doi: [10.1039/A606455H](https://doi.org/10.1039/A606455H)

534 Gale JD, Rohl AL (2003) The General Utility Lattice Program (GULP). *Molecular Simulation* 29:291–
535 341. doi: [10.1080/0892702031000104887](https://doi.org/10.1080/0892702031000104887)

536 Gatzemeier A, Wright K (2006) Computer modelling of hydrogen defects in the clinopyroxenes
537 diopside and jadeite. *Phys Chem Minerals* 33:115–125. doi: [10.1007/s00269-006-0059-0](https://doi.org/10.1007/s00269-006-0059-0)

538 Girard J, Chen J, Raterron P, Holyoke CW (2013) Hydrolytic weakening of olivine at mantle pressure:
539 Evidence of [1 0 0](0 1 0) slip system softening from single-crystal deformation experiments. *Physics*
540 *of the Earth and Planetary Interiors* 216:12–20. doi: [10.1016/j.pepi.2012.10.009](https://doi.org/10.1016/j.pepi.2012.10.009)

541 Hilairet N, Wang Y, Sanehira T, et al (2012) Deformation of olivine under mantle conditions: An in situ
542 high-pressure, high-temperature study using monochromatic synchrotron radiation. *J Geophys Res*
543 117:B01203. doi: [10.1029/2011JB008498](https://doi.org/10.1029/2011JB008498)

544 Idrissi H, Bollinger C, Boioli F, et al (2016) Low-temperature plasticity of olivine revisited with in situ
545 TEM nanomechanical testing. *Science Advances* 2:e1501671. doi: [10.1126/sciadv.1501671](https://doi.org/10.1126/sciadv.1501671)

546 Jaoul O, Bertran-Alvarez Y, Liebermann RC, Price GD (1995) Fe–Mg interdiffusion in olivine up to 9
547 GPa at T = 600–900°C; experimental data and comparison with defect calculations. *Physics of the*
548 *Earth and Planetary Interiors* 89:199–218. doi: [10.1016/0031-9201\(94\)03008-7](https://doi.org/10.1016/0031-9201(94)03008-7)

549 Katayama I, Karato S (2008) Low-temperature, high-stress deformation of olivine under water-
550 saturated conditions. *Physics of the Earth and Planetary Interiors* 168:125–133. doi:
551 [10.1016/j.pepi.2008.05.019](https://doi.org/10.1016/j.pepi.2008.05.019)

552 Keefner JW, Mackwell SJ, Kohlstedt DL, Heidelbach F (2011) Dependence of dislocation creep of
553 dunite on oxygen fugacity: Implications for viscosity variations in Earth’s mantle. *J Geophys Res*
554 116:B05201. doi: [10.1029/2010JB007748](https://doi.org/10.1029/2010JB007748)

555 Keller RJ, Mitchell TE, Heuer AH (1988) Plastic deformation in nonstoichiometric UO_{2+x} single
556 crystals—I. Deformation at low temperatures. *Acta Metallurgica* 36:1061–1071. doi: [10.1016/0001-](https://doi.org/10.1016/0001-6160(88)90160-5)
557 [6160\(88\)90160-5](https://doi.org/10.1016/0001-6160(88)90160-5)

558 Kelley KA, Cottrell E (2009) Water and the Oxidation State of Subduction Zone Magmas. *Science*
559 325:605–607. doi: [10.1126/science.1174156](https://doi.org/10.1126/science.1174156)

560 Kohlstedt DL, Keppler H, Rubie DC (1996) Solubility of water in the α , β and γ phases of
561 $(\text{Mg,Fe})_2\text{SiO}_4$. *Contrib Mineral Petrol* 123:345–357. doi: [10.1007/s004100050161](https://doi.org/10.1007/s004100050161)

562 Kröger FA, Vink HJ (1956) Relations between the Concentrations of Imperfections in Crystalline
563 Solids. *Solid State Physics* 3:307–435. doi: [10.1016/S0081-1947\(08\)60135-6](https://doi.org/10.1016/S0081-1947(08)60135-6)

564 Lauzier J, Hillairet J, Vieux-Champagne A, Benoit W (1989) The vacancies, lubrication agents of
565 dislocation motion in aluminium. *J Phys: Condens Matter* 1:9273. doi: [10.1088/0953-8984/1/47/001](https://doi.org/10.1088/0953-8984/1/47/001)

566 Leeuw NH de, Parker SC, Catlow CRA, Price GD (2000) Modelling the effect of water on the surface
567 structure and stability of forsterite. *Phys Chem Min* 27:332–341. doi: [10.1007/s002690050262](https://doi.org/10.1007/s002690050262)

568 Lewis GV, Catlow CRA (1985) Potential models for ionic oxides. *J Phys C: Solid State Phys* 18:1149.
569 doi: [10.1088/0022-3719/18/6/010](https://doi.org/10.1088/0022-3719/18/6/010)

570 Liao H, Xu Z (2015) Approaches to manage hesitant fuzzy linguistic information based on the cosine
571 distance and similarity measures for HFLTSs and their application in qualitative decision making.
572 *Expert Systems with Applications* 42:5328–5336. doi: [10.1016/j.eswa.2015.02.017](https://doi.org/10.1016/j.eswa.2015.02.017)

573 Lu G, Zhang Q, Kioussis N, Kaxiras E (2001) Hydrogen-Enhanced Local Plasticity in Aluminum: An
574 Ab Initio Study. *Phys Rev Lett* 87:095501. doi: [10.1103/PhysRevLett.87.095501](https://doi.org/10.1103/PhysRevLett.87.095501)

575 Lu G, Kaxiras E (2002) Can Vacancies Lubricate Dislocation Motion in Aluminum? *Phys Rev Lett*
576 89:105501. doi: [10.1103/PhysRevLett.89.105501](https://doi.org/10.1103/PhysRevLett.89.105501)

577 Mackwell SJ, Kohlstedt DL, Paterson MS (1985) The role of water in the deformation of olivine single
578 crystals. *J Geophys Res* 90:11319–11333. doi: [10.1029/JB090iB13p11319](https://doi.org/10.1029/JB090iB13p11319)

579 Mahendran S, Carrez P, Groh S, Cordier P (2017) Dislocation modelling in Mg_2SiO_4 forsterite: an
580 atomic-scale study based on the THB1 potential. *Modelling Simul Mater Sci Eng* 25:054002. doi:
581 [10.1088/1361-651X/aa6efa](https://doi.org/10.1088/1361-651X/aa6efa)

582 Martin RF, Donnay G (1972) Hydroxyl in the mantle. *American Mineralogist* 57:554–570

583 Miller MK (2006) Atom probe tomography characterization of solute segregation to dislocations and
584 interfaces. *J Mater Sci* 41:7808–7813. doi: [10.1007/s10853-006-0518-5](https://doi.org/10.1007/s10853-006-0518-5)

585 Nakamura A, Schmalzried H (1983) On the nonstoichiometry and point defects of olivine. *Phys Chem*
586 *Minerals* 10:27–37. doi: [10.1007/BF01204323](https://doi.org/10.1007/BF01204323)

587 Nguyen HV, Bai L (2010) Cosine Similarity Metric Learning for Face Verification. In: *Computer*
588 *Vision – ACCV 2010*. Springer, Berlin, Heidelberg, pp 709–720

589 Peterman EM, Reddy SM, Saxey DW, et al (2016) Nanogeochronology of discordant zircon measured
590 by atom probe microscopy of Pb-enriched dislocation loops. *Science Advances* 2:e1601318. doi:
591 [10.1126/sciadv.1601318](https://doi.org/10.1126/sciadv.1601318)

592 Price GD, Parker SC, Leslie M (1987) The lattice dynamics and thermodynamics of the Mg₂SiO₄
593 polymorphs. *Phys Chem Minerals* 15:181–190. doi: [10.1007/BF00308782](https://doi.org/10.1007/BF00308782)

594 Sanchez JM, Ducastelle F, Gratias D (1984) Generalized cluster description of multicomponent
595 systems. *Physica A: Statistical Mechanics and its Applications* 128:334–350. doi: [10.1016/0378-](https://doi.org/10.1016/0378-4371(84)90096-7)
596 [4371\(84\)90096-7](https://doi.org/10.1016/0378-4371(84)90096-7)

597 Sanders MJ, Leslie M, Catlow CRA (1984) Interatomic potentials for SiO₂. *J Chem Soc, Chem*
598 *Commun* 1271–1273. doi: [10.1039/C39840001271](https://doi.org/10.1039/C39840001271)

599 Schröder K-P, Sauer J, Leslie M, et al (1992) Bridging hydroxyl groups in zeolitic catalysts: a computer
600 simulation of their structure, vibrational properties and acidity in protonated faujasites (H⁺Y zeolites).
601 *Chemical Physics Letters* 188:320–325. doi: [10.1016/0009-2614\(92\)90030-Q](https://doi.org/10.1016/0009-2614(92)90030-Q)

602 Sinclair JE (1971) Improved Atomistic Model of a bcc Dislocation Core. *Journal of Applied Physics*
603 42:5321–5329. doi: [10.1063/1.1659943](https://doi.org/10.1063/1.1659943)

604 Smyth JR, Frost DJ, Nestola F, et al (2006) Olivine hydration in the deep upper mantle: Effects of
605 temperature and silica activity. *Geophys Res Lett* 33:L15301. doi: [10.1029/2006GL026194](https://doi.org/10.1029/2006GL026194)

606 Sommer H, Regenauer-Lieb K, Gasharova B, Siret D (2008) Grain boundaries: a possible water
607 reservoir in the Earth's mantle? *Miner Petrol* 94:1–8. doi: [10.1007/s00710-008-0002-9](https://doi.org/10.1007/s00710-008-0002-9)

608 Song W, Li CH, Park SC (2009) Genetic algorithm for text clustering using ontology and evaluating the
609 validity of various semantic similarity measures. *Expert Systems with Applications* 36:9095–9104. doi:
610 [10.1016/j.eswa.2008.12.046](https://doi.org/10.1016/j.eswa.2008.12.046)

611 Stocker RL, Smyth DM (1978) Effect of enstatite activity and oxygen partial pressure on the point-
612 defect chemistry of olivine. *Physics of the Earth and Planetary Interiors* 16:145–156. doi:
613 [10.1016/0031-9201\(78\)90085-7](https://doi.org/10.1016/0031-9201(78)90085-7)

614 Stroh AN (1958) Dislocations and Cracks in Anisotropic Elasticity. *Philosophical Magazine* 3:625–646.
615 doi: [10.1080/14786435808565804](https://doi.org/10.1080/14786435808565804)

616 Taketomi S, Matsumoto R, Miyazaki N (2008) Atomistic simulation of the effects of hydrogen on the
617 mobility of edge dislocation in alpha iron. *J Mater Sci* 43:1166–1169. doi: [10.1007/s10853-007-2364-5](https://doi.org/10.1007/s10853-007-2364-5)

618 Walker AM, Gale JD, Slater B, Wright K (2005a) Atomic scale modelling of the cores of dislocations
619 in complex materials part 1: methodology. *Phys Chem Chem Phys* 7:3227–3234. doi:
620 [10.1039/B505612H](https://doi.org/10.1039/B505612H)

621 Walker AM, Gale JD, Slater B, Wright K (2005b) Atomic scale modelling of the cores of dislocations
622 in complex materials part 2: applications. *Phys Chem Chem Phys* 7:3235–3242. doi:
623 [10.1039/B505716G](https://doi.org/10.1039/B505716G)

624 Walker AM, Demouchy S, Wright K (2006) Computer modelling of the energies and vibrational
625 properties of hydroxyl groups in α - and β -Mg₂SiO₄. *European Journal of Mineralogy* 18:529–543. doi:
626 [10.1127/0935-1221/2006/0018-0529](https://doi.org/10.1127/0935-1221/2006/0018-0529)

627 Walker AM, Woodley SM, Slater B, Wright K (2009) A computational study of magnesium point
628 defects and diffusion in forsterite. *Physics of the Earth and Planetary Interiors* 172:20–27. doi:
629 [10.1016/j.pepi.2008.04.001](https://doi.org/10.1016/j.pepi.2008.04.001)

630 Wright K, Catlow CRA (1994) A computer simulation study of (OH) defects in olivine. *Phys Chem*
631 *Minerals* 20:515–518. doi: [10.1007/BF00203222](https://doi.org/10.1007/BF00203222)

632 Zunger A, Wei S-H, Ferreira LG, Bernard JE (1990) Special quasirandom structures. *Phys Rev Lett*
633 65:353–356. doi: [10.1103/PhysRevLett.65.353](https://doi.org/10.1103/PhysRevLett.65.353)

635 **Tables**

636 **Table 1** Calculated core energies and elastic energy coefficients and core energies for the most stable
 637 configurations of dislocations in forsterite

	E_{core} (eV/Å)	K (GPa)
[100](010) edge dislocation	2.42±0.04	135.0
[001](010) edge dislocation	2.46±0.07	92.3
[100] screw dislocation	1.78±0.02	79.1
[001] screw dislocation	1.50±0.03	57.4

638

639 **Table 2** Minimum segregation energies (in eV) for defects around dislocations in forsterite. In each of these
 640 cases, the minimum energy site is close to the dislocation core, where atomic-scale effects dominate over elastic
 641 terms such the size-effect and inhomogeneity interactions

	[100](010) edge dislocation	[100] screw dislocation	[001](010) edge dislocation	[001] screw dislocation
$\{V_{M1}\}''$	-3.00	-0.87	-1.74	-0.76
$\{2H_{M1}\}^X$	-2.30	-1.00	-1.08	-0.89
$\{V_{M2}\}''$	-3.93	-1.91	-3.64	-1.89
$\{2H_{M2}\}^X$	-1.82	-2.46	-3.07	-1.73

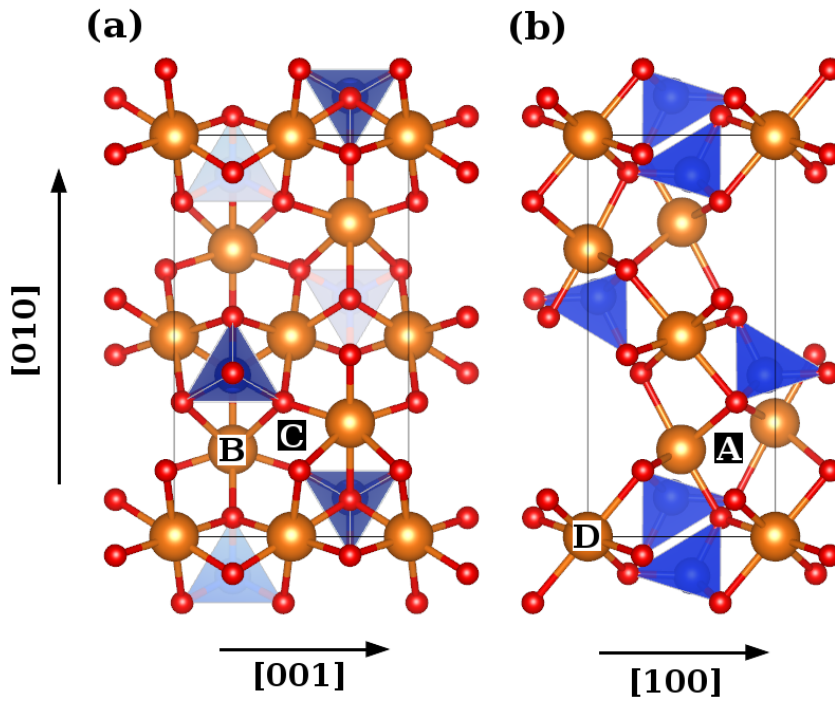
642

643 **Table 3** Values of the cosine similarity measure for bare and protonated M sites around the various dislocations
 644 in forsterite

	[100](010) edge dislocation	[100] screw dislocation	[001](010) edge dislocation	[001] screw dislocation
M1	0.89	0.78	0.81	0.73
M2	0.86	0.89	0.68	0.87

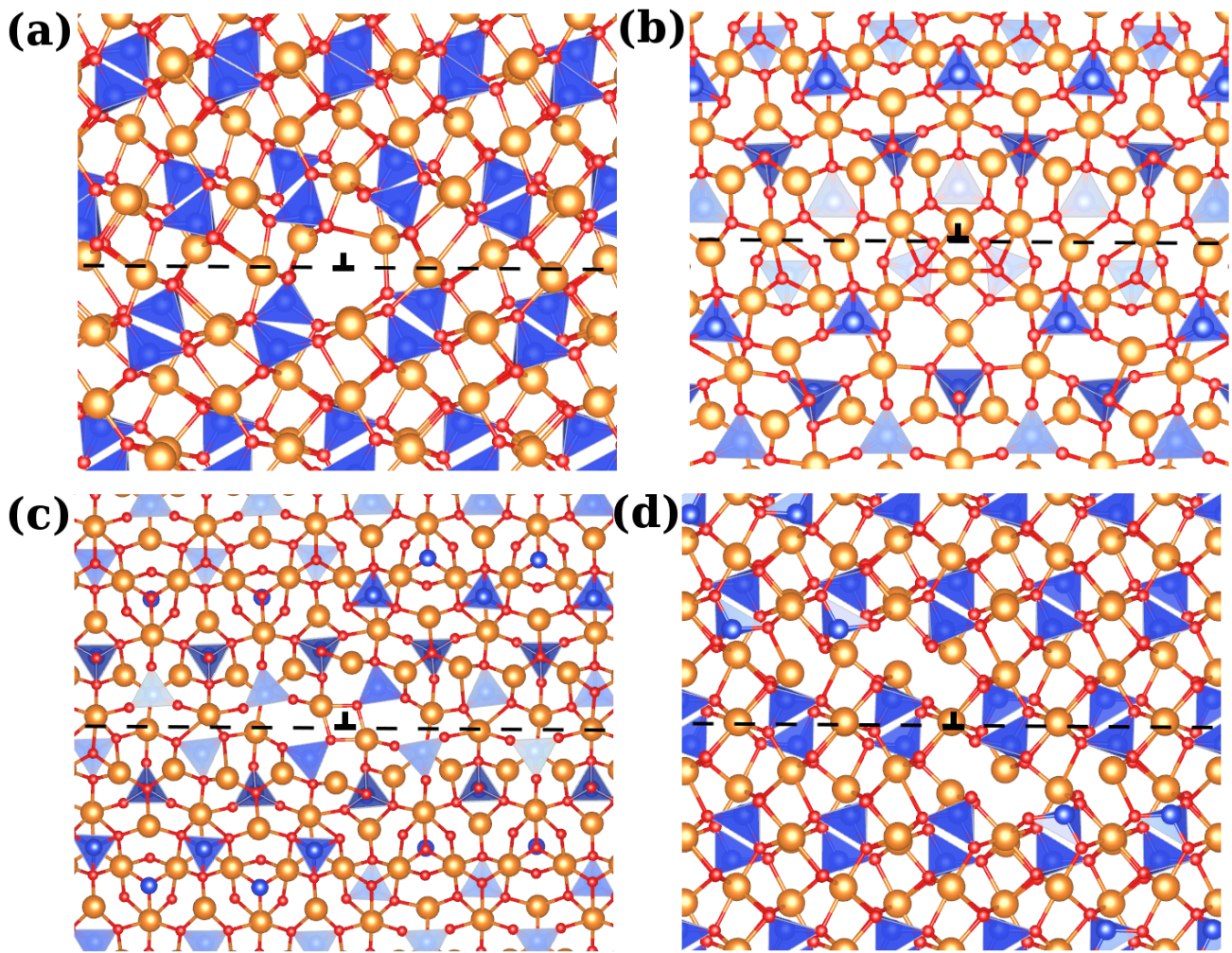
645

646



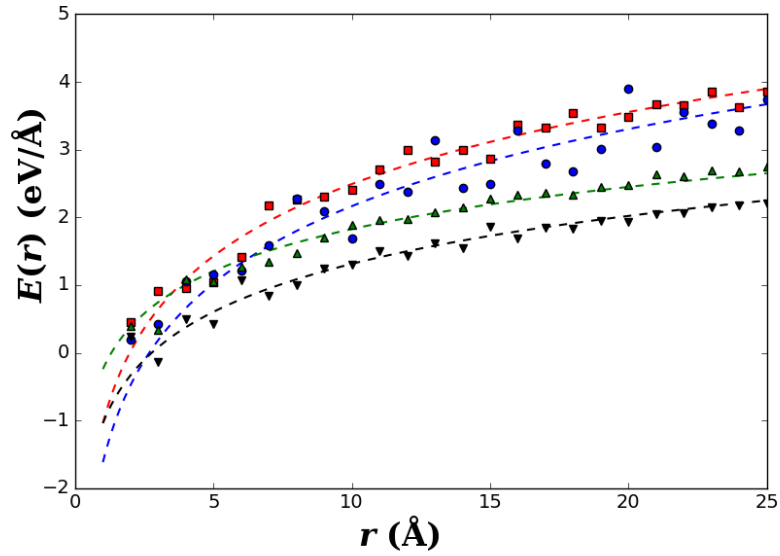
648

649 **Fig. 1** Olivine unit cell viewed down (a) the [100] cell direction, and (b) the [001] cell direction. Locations A, B,
650 C, and D are, respectively, the points in the unit cell through which the most stable core structures for the [100]
651 (010) edge, [001](010) edge, [100] screw, and [001] screw dislocations pass. Visualization produced using
652 VESTA 3 (Momma and Izumi 2011).



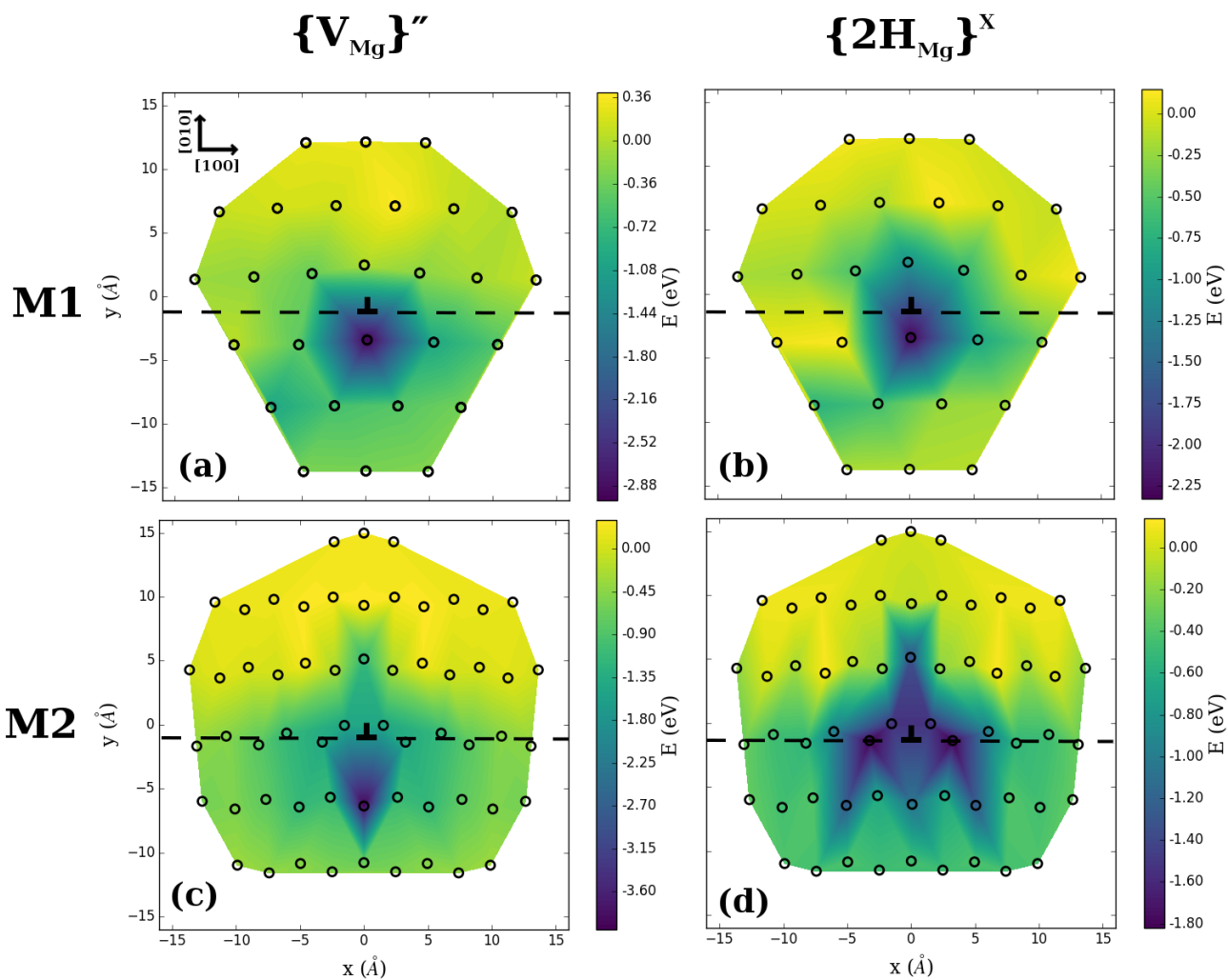
653

654 **Fig. 2** Atomic structures for the most stable core polymorphs of the (a) $[100](010)$ and (b) $[001](010)$ edge
 655 dislocations, and (c) $[100]$ and (d) $[001]$ screw dislocations in forsterite. The dislocation line and (010) glide
 656 plane have been marked. Visualization produced using VESTA 3 (Momma and Izumi 2011).



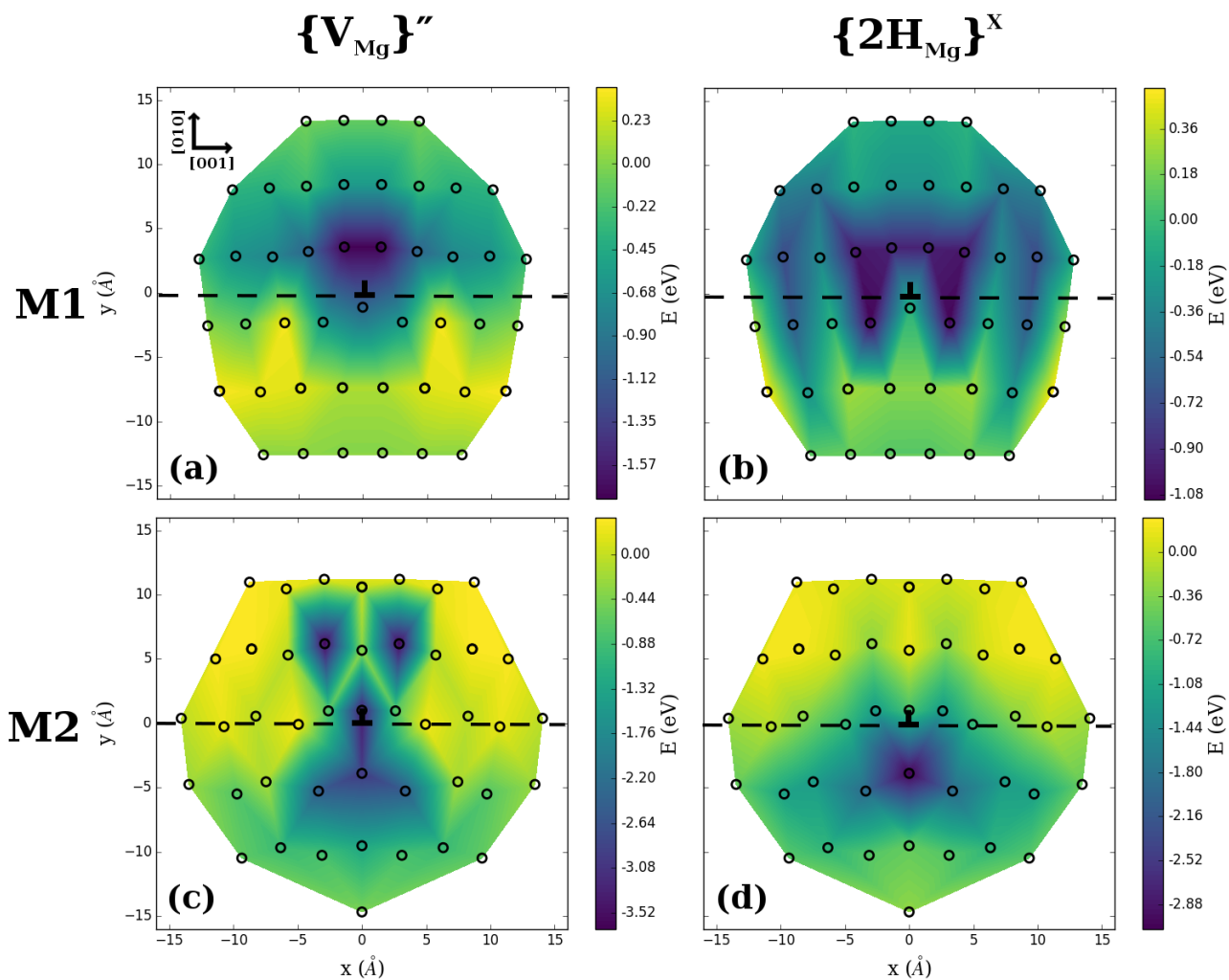
657

658 **Fig. 3** Dislocation line energies as a function of distance r from the dislocation line, together with the energy
 659 curve fitted using equation (1). [100](010) edge, [001](010) edge, [100] screw, and [001] screw dislocations
 660 energies are shown using squares, circles, triangles, and inverted triangles, respectively.



661

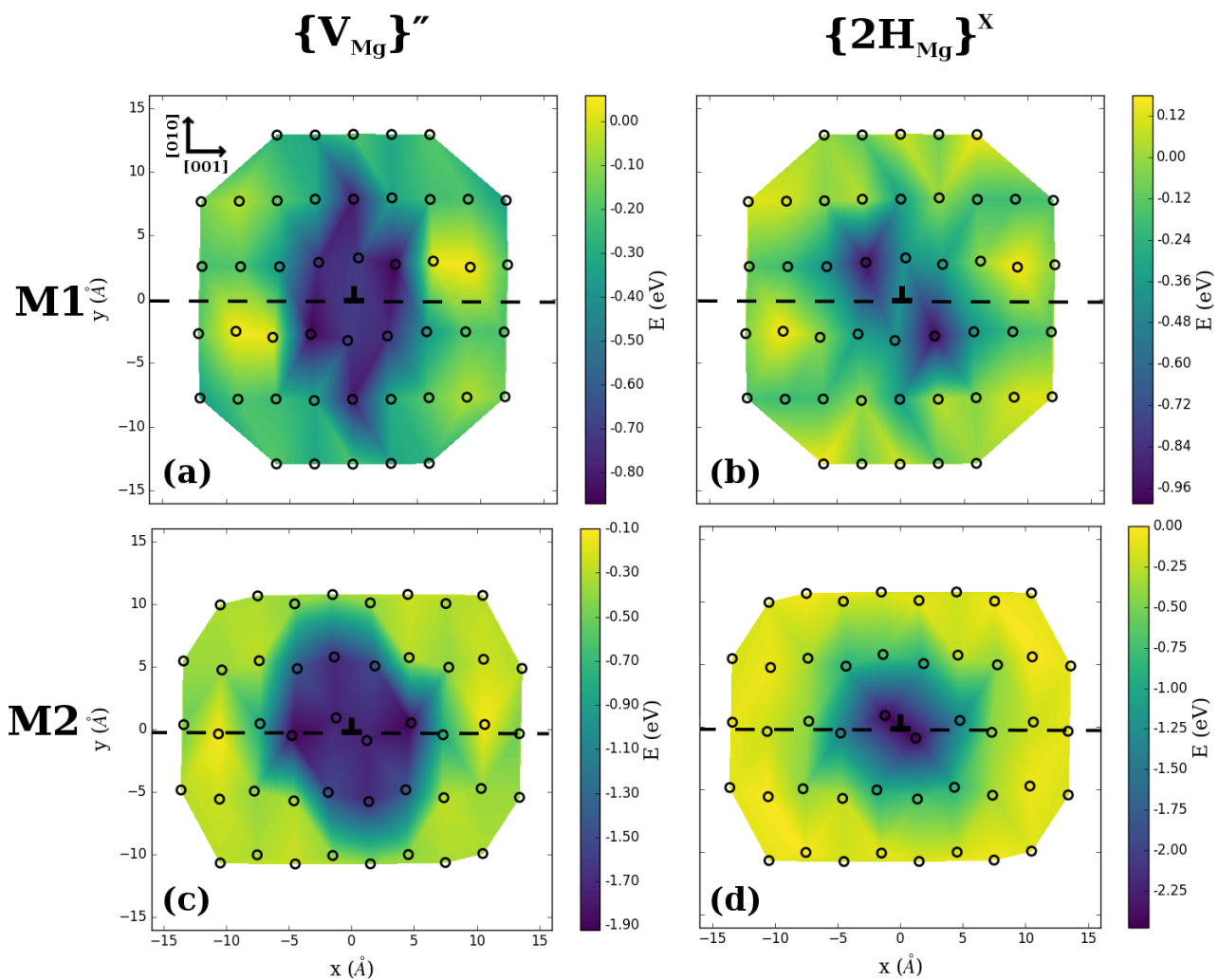
662 **Fig. 4** Segregation energies of bare and protonated Mg vacancies to the forsterite [100](010) edge dislocation.
 663 The [001] lattice vector is normal to the image plane. Note that segregation energies for M2 defects are
 664 computed relative to the corresponding defect in the bulk lattice, and are generally higher in energy than M1
 665 defects. Both the dislocation line and (010) glide plane are displayed.



666

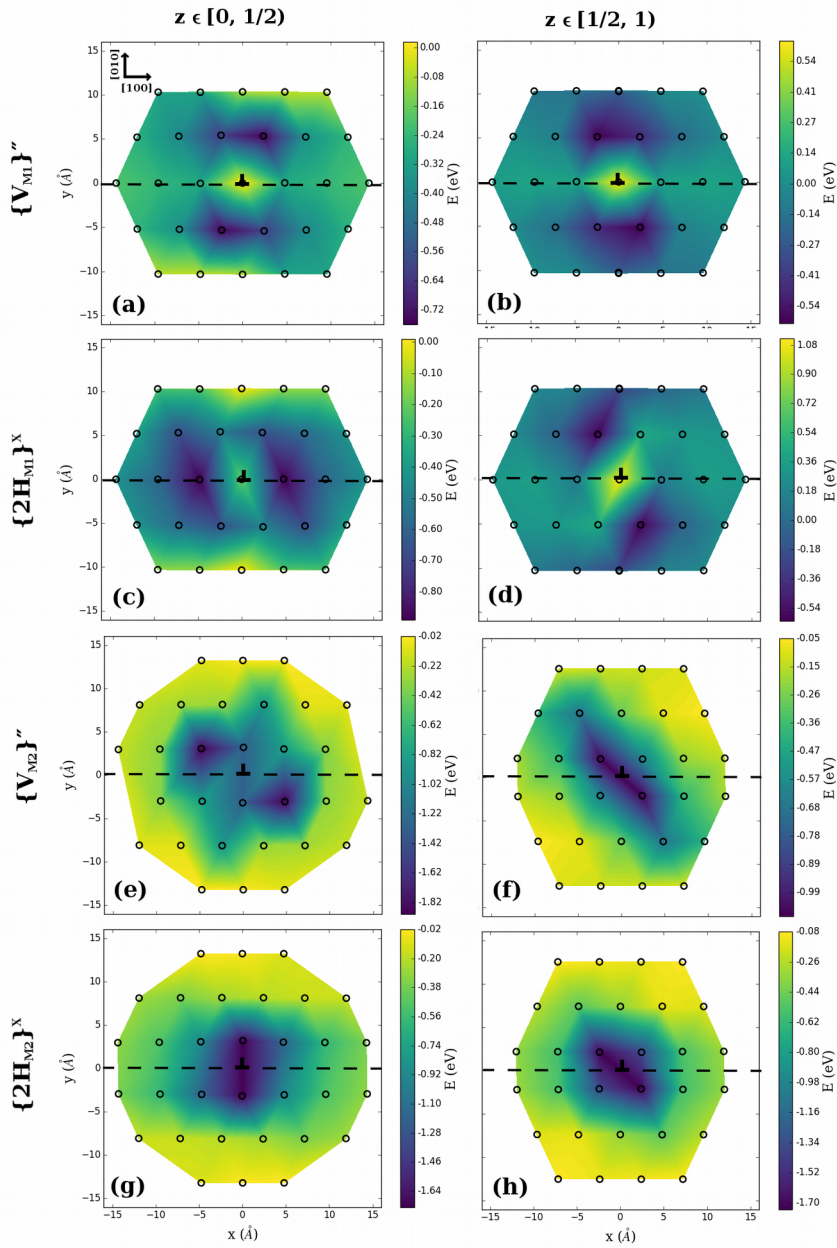
667 **Fig. 5** Segregation energies of bare and protonated Mg vacancies to the forsterite [001](010) edge dislocation.

668 The [100] lattice vector is normal to the image plane.



669

670 **Fig. 6** Segregation energies of bare and protonated Mg vacancies to the forsterite [100] screw dislocation. The
 671 [100] lattice vector is normal to the image plane.



672

673 **Fig. 7** Segregation energies of Mg vacancies to atomic sites around [001] screw dislocations. To reflect the
 674 modulated crystal structure of this dislocation along x , segregation energies for the "lower" ($z \in [0, 0.5)$) and
 675 "upper" ($z \in [0.5, 1.0)$) regions are plotted separately.